Attosecond timing of the dynamical Franz–Keldysh effect

JPhys Photonics

PAPER

Attosecond timing of the dynamical Franz–Keldysh effect

M Lucchini[1,2], S A Sato[3,4], F Schlaepfer[2], K Yabana[3,5], L Gallmann[2], A Rubio[4,6] and U Keller[2]

[1] Department of Physics, Politecnico di Milano, 20133 Milano, Italy
[2] Department of Physics, ETH Zurich, 8093 Zürich, Switzerland
[3] Center for Computational Sciences, University of Tsukuba, Tsukuba 305-8577, Japan
[4] Max Planck Institute for the Structure and Dynamics of Matter, Luruper Chaussee 149, 22761 Hamburg, Germany
[5] Graduate School of Pure and Applied Sciences, University of Tsukuba, Tsukuba 305-8571, Japan
[6] Center for Computational Quantum Physics (CCQ), The Flatiron Institute, 162 Fifth Avenue, New York, NY 10010, United States of America

E-mail: matteo.lucchini@polimi.it

OPEN ACCESS

RECEIVED
4 December 2019

REVISED
8 January 2020

ACCEPTED FOR PUBLICATION
28 January 2020

PUBLISHED
18 February 2020

Keywords: attosecond science, light–matter interaction, strong-field physics

Abstract

To what extent do intra- or inter-band transitions dominate the optical response of dielectrics when pumped by a few-cycle near-infrared transient electric field? In order to find an answer to this question we investigate the dynamical Franz–Keldysh effect in polycrystalline diamond and discuss in detail the attosecond delay of the induced electron dynamics with regard to the driving transient electric field while the peak intensity is varied between 1×10^{12} and 10×10^{12} W cm^{-2}. We found that the main oscillating feature in transient absorption at 43 eV is in phase with the electric field of the pump, to within 49 ± 78 as. However, the phase delay shows a slightly asymmetric V-shaped linear energy dispersion with a rate of about 200 as eV^{-1}. Theoretical calculations within the dipole approximation reproduce the data and allow us to conclude that intra-band motion dominates under our experimental conditions.

1. Introduction

The recent development of spectroscopic techniques based on attosecond extreme-ultraviolet (XUV) pulses has given us the ability to follow the ultrafast electron motion in solids that underlies fundamental processes of light–matter interaction. Besides photoelectron spectroscopy [1–4], all-optical techniques like attosecond transient absorption spectroscopy (ATAS) [5] have shown their potential for the investigation of fundamental phenomena in semiconductors [6], dielectrics [7], metals [8] and magnetic systems [9], up to petahertz driving fields [10]. The first pioneering experiments brought unprecedented insights in strong-field physics in solid systems, addressing the role of inter- and intra-band excitation from a new perspective [11–13]. Nevertheless, the exact interplay between virtual and real electron dynamics on attosecond time scales is far from being completely understood. In this work we used ATAS in combination with a precise external time-delay calibration in order to study the timing of virtual carrier dynamics, namely the dynamical Franz–Keldysh effect (DFKE) [14], in polycrystalline diamond pellicles as a function of peak intensity of the optical pump. The intensity regime under investigation is within the dipole approximation where we can neglect the magnetic field interaction [15, 16].

DFKE is a fast non-resonant process in which an external field is used to modify the potential landscape of dielectrics in a way such that photon absorption can occur below the optical absorption edge. Often described as photo-assisted tunneling [18], DFKE is normally observed around the energy gap of dielectrics in the terahertz regime [19] (figure 1). We recently demonstrated that the DFKE can also be induced between sub-bands deep into the conduction bands, reaching the petahertz domain [11]. In particular, one can use attosecond pulses with a spectrum that extends between 30 and 60 eV to probe a region of the optical response of diamond dominated by transitions between the first and the eleventh sub-bands (figure 1(d)). Control over the transition probability between the sub-bands through virtual carriers is obtained with a moderately intense ($I_p^{IR} \simeq 1 \times 10^{12}$ W cm^{-2}) femtosecond IR pulse for which the carrier-envelope offset is stabilized [20]. The diamond transient absorption

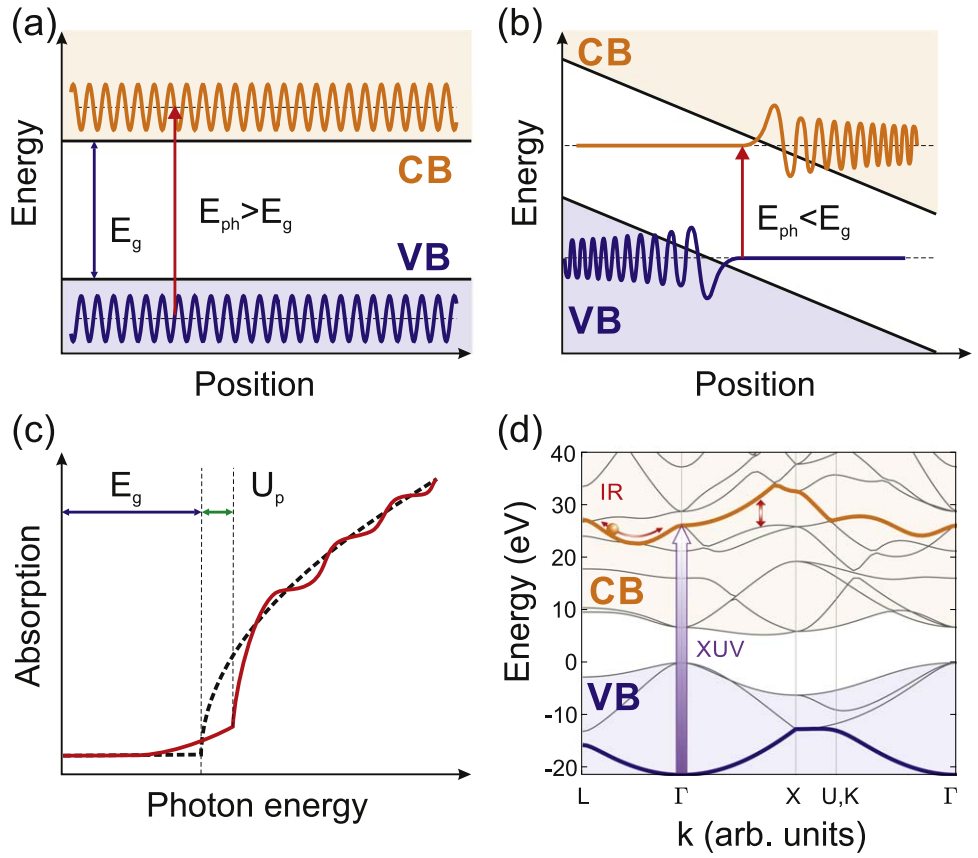

Figure 1. (**a**) Schematic of two electronic states in the valence band (VB) and conduction band (CB). Electron wave-functions are represented by periodic Bloch functions and photon absorption can only occur for photon energies bigger than the energy gap $E_{ph} \geqslant E_g$. (**b**) The same situation in the presence of an external field. The external field bends the potential, Bloch functions are no longer a solution of the Hamiltonian and absorption can occur for $E_{ph} < E_g$. (**c**) Schematic of the absorption profile around E_g in the static case (black dashed curve) and in case of DFKE (red solid curve) [17]. In the latter case, one can observe non-zero absorption below E_g, a shift of the absorption edge proportional to the field quiver energy U_p and oscillations in the absorption profile. (**d**) Diamond band diagram showing the main involved sub-bands of the CB and VB. While the XUV photons probe the transition between the first and eleventh sub-bands (thicker lines), the IR can either accelerate electrons within the same sub-band (intra-band motion) or project electrons vertically into another sub-band (inter-band transition).

shows features that oscillate with twice the IR frequency and a characteristic V-shaped energy-dependent dispersion. As the process takes place when an adiabaticity parameter, γ_a [21], defined as the ratio between the ponderomotive and the photon energy of the field, is around 1, the field cannot be treated solely as a classical wave or as an ensemble of photons [22]. Thus the physical mechanism taking place cannot be completely described by vertical inter-band transitions (photon picture) or intra-band motion (classical field picture) alone, rendering the quest to finding an easy and intuitive mental image a formidable task. Otobe and co-workers predicted that the complex interplay between intra-band motion and inter-band transitions is expected to significantly affect the timing of the DFKE which should change with the pump intensity [21], thus suggesting a way to gain new insight into this complex mechanism. Our results show that, as long as the adiabaticity parameter γ_a is kept below 0.3, the timing of the observed dynamics does not depend on IR intensity.

The work is organized as follows: section 2 presents the experimental setup used to perform the ATAS measurements. The procedures used to extract precise timing information are reported in section 3. Section 4 contains the experimental and calculation results while the conclusions are in section 5.

2. Experimental setup

The experiments were performed at the Attoline setup at ETH Zurich [11, 23]. A schematic of the experimental configuration is presented in figure 2(a).

Single attosecond pulses (SAPs) with a time duration of about 250 as and a spectrum centered around 42.5 eV (figure 2(b)) were generated, exploiting the high-order harmomic generation process in combination with the polarization gating technique [24]. We optimized the XUV generation in order to have maximum flux around the strongest feature of the diamond transient absorbance [11] at 43 eV. As reported in the

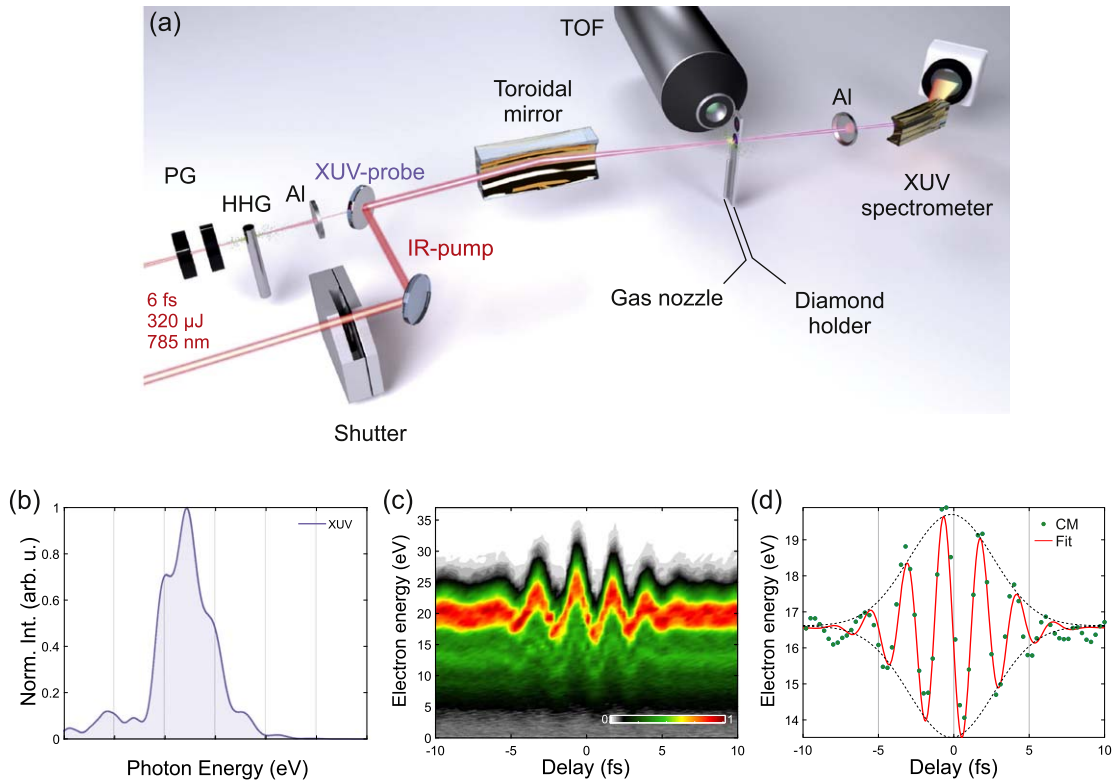

Figure 2. (**a**) Schematic of the experimental setup used for ATAS. (**b**) Attosecond pulse spectrum. (**c**) Streaking trace obtained in Ne with the pulse in (b). (**d**) Delay dependence of the photoelectron center of mass (CM) extracted from the trace in (c) (green dots). The red solid line represents a fit function, which is used to extract the negative IR vector potential: $-A_{IR}(t)$.

supplementary material of [11], the spectral shape of the attosecond radiation does not affect the experimental result as the same dynamics can also be observed with attosecond pulse trains. The 25-fs IR pulses at a central wavelength of 800 nm are shortened in a double-filament compression setup followed by a set of chirped mirrors. After compression, the IR pulses have a duration of about 6 fs and energy of ~320 μJ. The beam is then divided by an 80–20 beam splitter. The stronger part is used to generate the SAPs. The 20% fraction is instead used as a pump in our experiment and passes via a delay line before being collinearly recombined with the XUV radiation (probe) on a drilled mirror. Both beams are focused by a gold-plated toroidal mirror into the target region. The target consists of a gas nozzle, injecting Ne atoms, followed by a sample holder where the polycrystalline diamond pellicles are placed. The gas nozzle and the holder are placed in front of a time-of-flight spectrometer, which is used to simultaneously acquire Ne photoelectron spectra while performing the ATAS measurements. Figure 2(c) shows a typical attosecond streaking trace [25] obtained by collecting the photoelectron spectra from the Ne gas as a function of the SAP–IR delay. Besides giving precise timing information [26], one can use the streaking trace to reconstruct both the IR and XUV pulse profiles by means of frequency-resolved optical gating for the complete reconstruction of attosecond bursts (FROG-CRAB) [27]. Alternatively, the IR vector potential, $A_{IR}(t)$, can be directly extracted from the delay dependence of the center of mass of the streaking trace, as shown in figure 2(d) [28].

After passing through the 50-nm-thick diamond pellicles, the SAP spectrum is measured by an XUV spectrometer placed at the end of the beamline. A home-made shutter [29] operating at 40 Hz is mounted in the IR beam path in order to enable sequential acquisition of transmitted spectra with and without presence of the pump. This strongly increases the signal to noise ratio and allows us to evaluate the pump-induced changes in the diamond absorbance defined as follows: $\Delta Abs(E_{ph},\ t) = \ln\left(\frac{I_0(E_{ph})}{I_{IR}(E_{ph},\ t)}\right)$, where E_{ph} is the photon energy, t is the pump–probe delay and I_{IR}/I_0 is the transmitted XUV intensity with and without the IR pump.

3. Phase delay extraction

In order to investigate the DFKE in diamond, we measured the IR-induced absorbance $\Delta Abs(E_{ph}, t)$ for different IR peak intensities and extracted the precise timing between the main oscillating feature at 43 eV and the square of the pump vector potential, $A^2_{IR}(t)$.

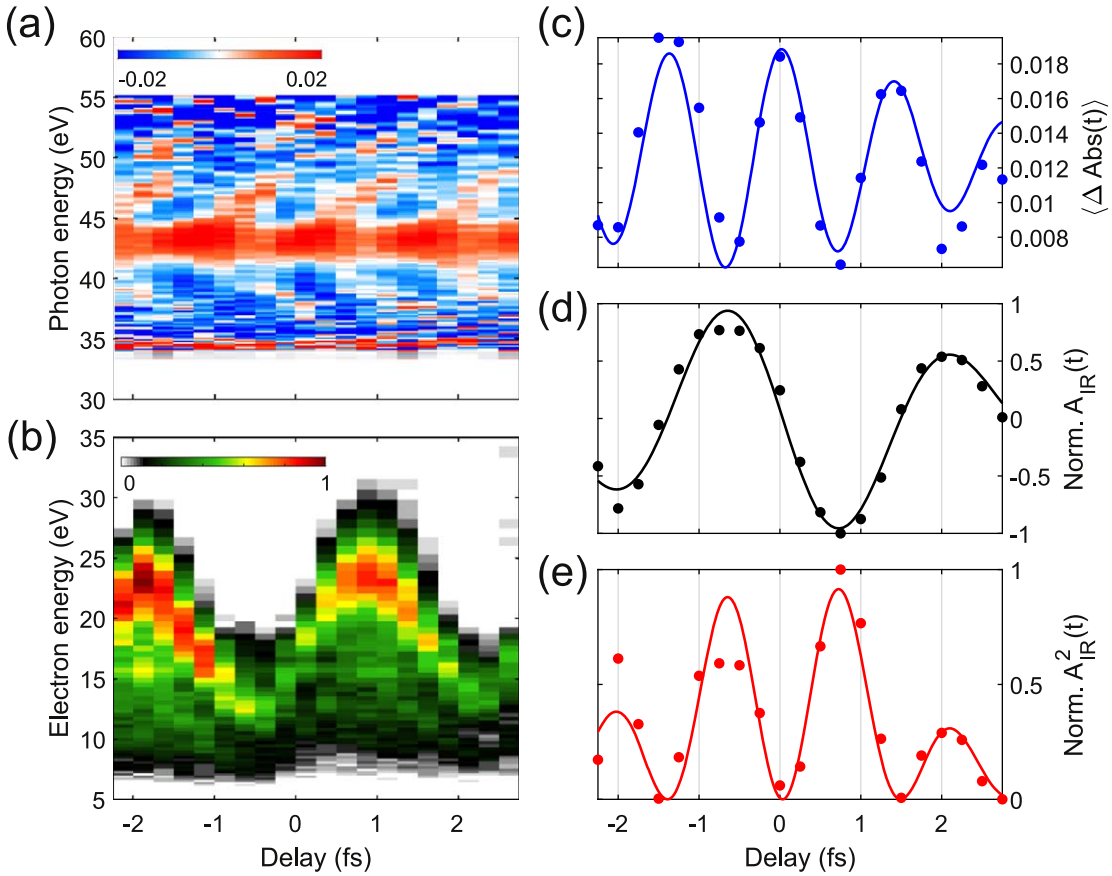

Figure 3. (**a**) IR-induced changes in the diamond absorbance, $\Delta Abs(E_{ph}, t)$ as a function of pump–probe delay. The IR intensity was set to 5.6×10^{12} W cm^{-2}. (**b**) Portion of the simultaneous streaking trace acquired in Ne. (**c**) $\langle \Delta Abs(t) \rangle$ averaged between 42.5 and 43.5 eV, showing clear oscillations at $2\omega_{IR}$. (**d**). IR vector potential $A_{IR}(t)$ (or its square (**e**)), extracted from the streaking trace in (b) and used for precise calibration of the transient features observed in (a).

Figure 3(a) shows an ATAS trace recorded with an IR peak intensity of $I_p^{IR} = 5.6 \times 10^{12}$ W cm^{-2}, while figure 3(b) displays the simultaneously recorded streaking trace in Ne. In figure 3(a) it is possible to recognize a V-shaped structure that oscillates with twice the IR optical frequency (ω_{IR}); this was previously identified as a fingerprint of the DFKE. We note that the attosecond probe pulse does not affect the IR-induced dynamics as its peak intensity is between three and four orders of magnitude smaller than I_p^{IR}, about 10^8–10^9 W cm^{-2}. This assumption is further sustained by the excellent agreement of our experimental data with theoretical models which neglect any probe-pulse-induced dynamics. In order to evaluate the effect of the pump intensity on the timing of the V-shaped structure, we concentrate on the strongest feature at 43 eV. We integrate the IR-induced absorbance in a range between 42.5 and 43.5 eV to obtain an energy-averaged response $\langle \Delta Abs(t) \rangle$ (figure 3(c)) and compare it with the square of the IR vector potential (figure 3(e)) evaluated following the center of mass (figure 3(d)) of the simultaneously recorded streaking trace (figure 3(b)).

We repeated the measurement by changing I_p^{IR} between 1.4×10^{12} and 10.5×10^{12} W cm^{-2}. Figure 4 shows three ATAS traces taken with (a) 1.6×10^{12} W cm^{-2}, (b), 5.8×10^{12} W cm^{-2} and (c), 10×10^{12} W cm^{-2}. The lower rows display $\langle \Delta Abs(t) \rangle$ and the square IR vector potential $A_{IR}^2(t)$. The V-shaped oscillating structure is observed for all pump intensities under examination. Below $I_p^{IR} = 1.4 \times 10^{12}$ W cm^{-2} the signal starts to be buried by the experimental noise, while above 10.5×10^{12} W cm^{-2} we observe permanent damage in the diamond pellicles (ablation) during the measurement time (typically 1 h for this limited delay range). We found the amplitude of the main oscillating features to scale almost linearly with the IR pump intensity, while the oscillation timing does not change significantly. In order to extract the phase difference between the blue and red curves in figure 4, we followed the approach reported in [26]. We Fourier transform both $\langle \Delta Abs(t) \rangle$ and $A_{IR}^2(t)$ and multiply one by the complex conjugate of the other. The amplitude of the product, $P(\omega)$, automatically peaks at the common frequency between the two signals and its phase gives directly the phase difference $\Delta\phi(\omega)$ between the two. The mean phase delay $\langle \Delta\tau \rangle$ is then obtained by averaging $\Delta\tau(\omega) = \Delta\phi(\omega)/\omega$ over the spectral weight of Fourier transform product $P(\omega)$ as follows: $\langle \Delta\tau \rangle = \int P(\omega)\Delta\tau(\omega)d\omega / \int P(\omega)d\omega$. In the same fashion, for each measurement, an estimate of the measurement error is then given by the standard deviation weighted by $P(\omega)$.

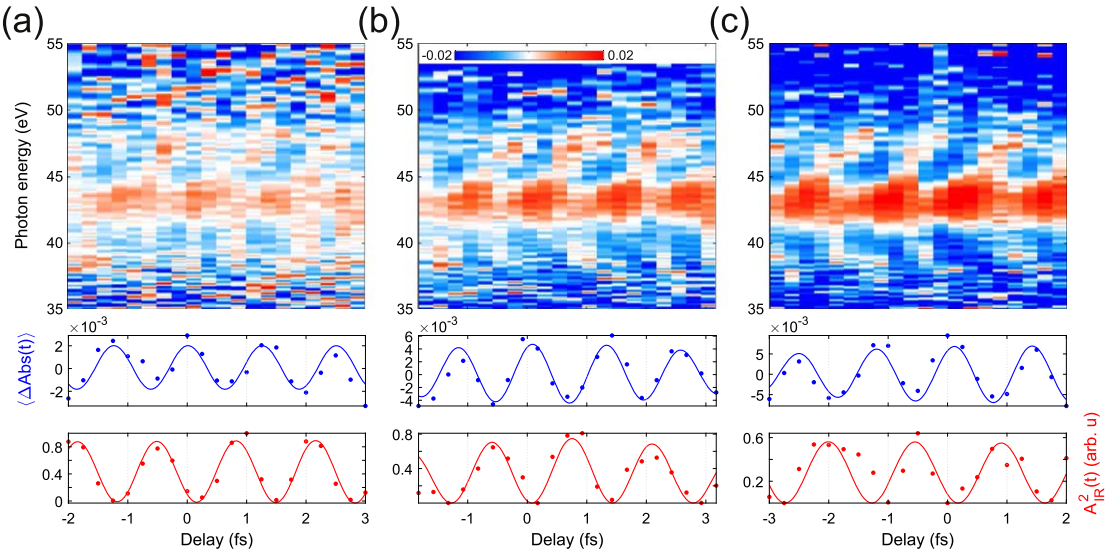

Figure 4. First row, transient absorbance $\Delta Abs(E_{ph}, t)$ of diamond for a peak IR intensity, I_p^{IR}, of (**a**) 1.6 $\times$ 10^{12}, (**b**) 5.8 $\times$ 10^{12} and (**c**) 1 $\times$ 10^{13} W cm^{-2}. The second and third rows display $\langle \Delta A(t) \rangle$ calculated between 42.5 and 43.5 eV and the associated $A_{IR}^2(t)$ extracted from simultaneously recorded streaking traces.

4. Experimental and theoretical results

The measured phase delays between the main oscillating feature at 43 eV and the IR electric field, or vector potential, are reported in figure 5(a). We performed a total of 53 ATAS measurements with different IR intensities (gray dots and error bars), which are grouped in six IR intensity regions. The blue dots represent the average phase delay for each region. Average and error bars are calculated weighting each individual measured point by the inverse of its uncertainty. As already mentioned in the previous section, we observed no significant change of the phase delay within the investigated intensity range. The total average of all the measurements gives statistically a zero phase delay between the main feature at 43 eV and the IR electric field, $\langle \Delta\tau_E \rangle$ of 49 $\pm$ 78 as. Therefore we can conclude that the main oscillating feature in $\Delta Abs(E_{ph}, t)$ is in phase with the pump electric field $E_{IR}(t)$. Moving away from the energy center of the V-shaped structure at 43 eV, the phase delay changes rapidly with the photon energy E_{ph}. Figure 5(b) shows the energy-dependent phase delay $\Delta\tau_E$ extracted from the ATAS trace of figure 3(a). Above 43 eV the phase delay follows a linear dispersion with a positive slope of 191 $\pm$ 4 as eV^{-1} (orange dashed line). Below 43 eV instead, $\Delta\tau_E$ increases for a decreasing photon energy with a slightly higher slope of -230 $\pm$ 10 as eV^{-1} (red dash-dotted line).

In order to better understand the physical mechanism behind the observations, we performed first-principles ATAS simulations based on the combined theoretical framework of quantum electron dynamics and light-field propagation [30]. In the simulations, the quantum electron dynamics in solids is described by time-dependent density functional theory (TDDFT) [31] while the light-field propagation is described with Maxwell's equations. To simulate the whole experimental process, IR and XUV pulses are set in front of a 50-nm thick diamond film as an initial condition of the simulations. Then, we simulated the propagation of light fields through the diamond film and analyzed the spectrum of the transmitted XUV pulse. In the simulations we considered a pure crystal oriented along the (001) direction. As shown in [11], this does not affect the timing of the oscillation phase delay. By repeating the simulations with different time delays between IR and XUV pulses, the transient absorbance $\Delta Abs(E_{ph}, t)$ can be computed as a function of the pump–probe time delay.

To investigate the exact timing of the observed dynamics we first performed first-principles ATAS simulations with an IR intensity of $I_p^{IR} = 5 \times 10^{12}$ W cm^{-2} (figure 5(d)). The computed transient absorption scan is shown in figure 5(d). The phase of the part exhibiting 2ω oscillations shows a clear V-shaped structure which gives a phase delay in remarkable agreement with the experimental data (figure 5(b)). Indeed, the phase delay of the main oscillating feature between 41 and 42 eV is 45 $\pm$ 2 as and the extracted slopes for the upper and lower branch are 208 $\pm$ 4 and -247 $\pm$ 4 as eV^{-1}, respectively. Unfortunately a clear conclusion concerning the exact physical origin of the observed V-shaped phase delay dispersion is outside the scope of the present measurements on polycrystalline samples. Future work based on crystalline samples of different orientations, together with a comparison between different pump wavelengths, may allow us to disentangle the different mechanisms involved.

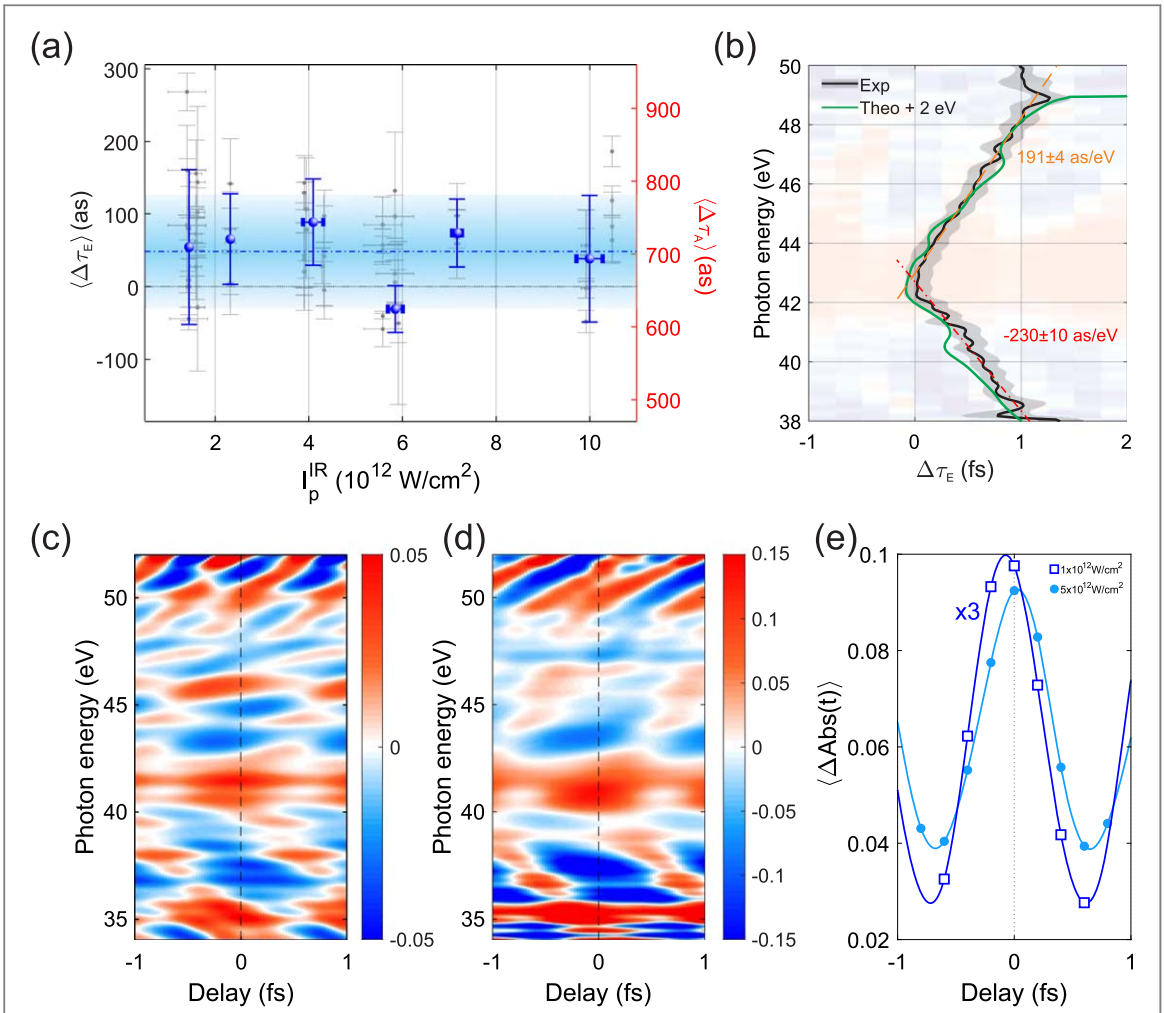

Figure 5. (**a**) Phase delay, $\langle \Delta\tau_E \rangle$, between $\langle \Delta Abs(t) \rangle$ at 43 eV (defined as in figure 3) and the pump electric field (right vertical axis) or its vector potential (left vertical axis), as a function of the IR peak intensity I_p^{IR}. Gray dots and error bars represent individual measurements. The blue dots represent the phase delay obtained by averaging all the measurements performed at the same IR intensity. The phase delay shows no appreciable dependence upon I_p^{IR}. The horizontal blue dashed line shows the average of all the measurements, 49 as, while the shaded light blue area covers twice the total standard deviation of 78 as. (**b**) Photon energy dispersion of the phase delay $\Delta\tau_E$ showing the V-shaped structure coming from the DFKE for experiment (black curve) and theory (green curve). The energy axis of the calculation results has been shifted by 2 eV upwards in for better comparison with the experimental data. In the background figure 3(a) is displayed. (**c**), (**d**) Calculated diamond single-cell transient absorption for $I_p^{IR} = 1 \times 10^{12}$ and $I_p^{IR} = 5 \times 10^{12}$ W cm^{-2}, respectively. (**e**) Calculated absorbance profile extracted from the main feature between 41 and 42 eV from (c) (blue open squares) and (d) (light blue dots).

In order to investigate the dependence on IR intensity we then repeated the calculations for $I_p^{IR} = 1 \times 10^{12}$ W cm^{-2}. The results are displayed in figure 5(c). Figure 5(e) shows the time-delay-dependent profile, obtained by integrating $\Delta Abs(E_{ph}, t)$ in the energy range between 41 and 42 eV. The change in phase delay observed in the theoretical results with varying I_p^{IR} in the investigated range is negligible on the scale of the ~70 as the uncertainty of our experiment.

In our previous work we demonstrated that the DFKE at 5×10^{12} W cm^{-2} can be qualitatively reproduced by either only two Houston states [32] or a two-level system. This allowed us to conclude that DFKE is dominated by intra-band motion. Here we conclude that this finding holds for the whole range of intensities studied.

5. Conclusions

In conclusion, we investigated the optical response to an 800 nm laser pulse (382 THz) in diamond in the attosecond regime, with particular focus on the precise timing between the energy-dependent transient absorption modulations and the pump electric field. We found a V-shaped energy-dependent delay in the response that can be fully explained by the DFKE. The central main oscillating feature at 43 eV, corresponding to the vertical transition between the first sub-band in the valence band and the eleventh sub-band in the

conduction band, is in phase with the pump electric field to within 49 ± 78 as and independent of pump peak intensity in the range between 1.4 and 10.5 × 10^{12} W cm^{-2}. The V-shaped energy dispersion is slightly asymmetric (figure 5(b)) with a linear dispersion of about 190 as eV^{-1} for larger photon energies and about −230 as eV^{-1} for smaller photon energies. These results are confirmed by first-principles electron dynamics simulations, highlighting the dominant role of intra-band motion in this regime. Our results suggest that the physical process responsible for the fast modulations in the optical response of diamond is robust and shows no significant dependence on the pump intensity. At first sight this seems to contradict the results of Otobe and co-workers [21], who predicted that the phase delay $\Delta\tau_E$ should change strongly with pump intensity. However, Otobe and co-workers used mid-IR pulses to investigate an interaction regime where the adiabaticity parameter γ_a ranged from 0.29 to 4.76. In our case we covered a range defined by $0.04 \leqslant \gamma_a \leqslant 0.3$. Here we have shown, both experimentally and theoretically, that for small γ_a, the timing of microscopic electronic motion is not qualitatively affected by the pump intensity. At 800 nm a higher pump pulse intensity introduces sample damage. Therefore one would need to use a longer wavelength transient electric field in the mid-IR to explore higher pump intensity regimes.

Acknowledgments

This research was supported by the NCCR MUST, funded by the Swiss National Science Foundation. This research used computational resources from the K computer provided by RIKEN AICS through the HPCI System Research project (project ID hp150101) and the Garching Supercomputing Center of the Max Planck Society.

ORCID iDs

M Lucchini https://orcid.org/0000-0001-6476-100X
S A Sato https://orcid.org/0000-0001-9543-2620

References

[1] Cavalieri A *et al* 2007 *Nature* **449** 1029–32
[2] Locher R, Castiglioni L, Lucchini M, Greif M, Gallmann L, Osterwalder J, Hengsberger M and Keller U 2015 *Optica* **2** 405–10
[3] Lucchini M, Castiglioni L, Kasmi L, Kliuiev P, Ludwig A, Greif M, Osterwalder J, Hengsberger M, Gallmann L and Keller U 2015 *Phys. Rev. Lett.* **115** 137401
[4] Kasmi L, Lucchini M, Castiglioni L, Kliuiev P, Osterwalder J, Hengsberger M, Gallmann L, Krüger P and Keller U 2017 *Optica* **4** 1492–7
[5] Geneaux R, Marroux H J B, Guggenmos A, Neumark D M and Leone S R 2019 *Phil. Trans. R. Soc.* A **377** 20170463
[6] Schultze M *et al* 2014 *Science* **346** 1348–52
[7] Schultze M *et al* 2012 *Nature* **493** 75–8
[8] Volkov M, Sato S A, Schlaepfer F, Kasmi L, Hartmann N, Lucchini M, Rubio A and Keller U 2019 *Nat. Phys.* **15** 1145–9
[9] Siegrist F *et al* 2019 *Nature* **571** 240–4
[10] Mashiko H, Oguri K, Yamaguchi T, Suda A and Gotoh H 2016 *Nat. Phys.* **12** 1–6
[11] Lucchini M, Sato S A, Ludwig A, Herrmann J, Volkov M, Kasmi L, Shinohara Y, Yabana K, Gallmann L and Keller U 2016 *Science* **353** 916–9
[12] Schlaepfer F, Lucchini M, Sato S A, Volkov M, Kasmi L, Hartmann N, Rubio A, Gallmann L and Keller U 2018 *Nat. Phys.* **14** 560–4
[13] Sato S A, Lucchini M, Volkov M, Schlaepfer F, Gallmann L, Keller U and Rubio A 2018 *Phys. Rev.* B **98** 035202
[14] Jauho A P and Johnsen K 1996 *Phys. Rev. Lett.* **76** 4576–9
[15] Reiss H R 2008 *Phys. Rev. Lett.* **101** 043002
[16] Ludwig A, Maurer J, Mayer B W, Phillips C R, Gallmann L and Keller U 2014 *Phys. Rev. Lett.* **113** 243001
[17] Srivastava A, Srivastava R, Wang J and Kono J 2004 *Phys. Rev. Lett.* **93** 157401
[18] Yu P Y and Cardona M 2010 *Fundamentals of Semiconductors* 4th edn (Berkeley, CA: Springer)
[19] Uchida K, Otobe T, Mochizuki T, Kim C, Yoshita M, Akiyama H, Pfeiffer L N, West K W, Tanaka K and Hirori H 2016 *Phys. Rev. Lett.* **117** 277402
[20] Telle H, Steinmeyer G, Dunlop A, Stenger J, Sutter D and Keller U 1999 *Appl. Phys.* B **69** 327–32
[21] Otobe T, Shinohara Y, Sato S A and Yabana K 2016 *Phys. Rev.* B **93** 045124
[22] Chin A H, Bakker J M and Kono J 2000 *Phys. Rev. Lett.* **85** 3293–6
[23] Locher R *et al* 2014 *Rev. Sci. Instrum.* **85** 013113
[24] Sansone G *et al* 2006 *Science* **314** 443–6
[25] Itatani J, Quéré F, Yudin G L, Ivanov M Y, Krausz F and Corkum P B 2002 *Phys. Rev. Lett.* **88** 173903
[26] Schlaepfer F, Ludwig A, Lucchini M, Kasmi L, Volkov M, Gallmann L and Keller U 2017 *Opt. Express* **25** 3646–55
[27] Mairesse Y and Quéré F 2005 *Phys. Rev.* A **71** 011401
[28] Kitzler M, Milosevic N, Scrinzi A, Krausz F and Brabec T 2002 *Phys. Rev. Lett.* **88** 173904
[29] Martínez S, Hernández L, Reyes D, Gomez E, Ivory M, Davison C and Aubin S 2011 *Rev. Sci. Instrum.* **82** 046102
[30] Yabana K, Sugiyama T, Shinohara Y, Otobe T and Bertsch G F 2012 *Phys. Rev.* B **85** 045134
[31] Runge E and Gross E K U 1984 *Phys. Rev. Lett.* **52** 997–1000
[32] Houston W V 1940 *Phys. Rev.* **57** 184–6